THE DYNAMIC BEHAVIOR OF THE COHERENT FLOW BETWEEN SHROUDED CO-ROTATING DISKS

Shen-Chun Wu and Yau-Ming Chen*

ABSTRACT

Time-resolved measurements were made to study large-scale structures between shrouded co-rotating disks in the present work. Two laser velocimeters and a phase-averaged technique were employed to investigate the dynamic behavior of the coherent structures. From the reconstructed streamline patterns, three distinct flow regions can be identified quantitatively: namely, an inner region nears the hub, an outer region, and a shroud boundary-layer region. The outer region is distinguished by the presence of large vortical structures and it is the most energetic region in the flow field. Using a triple decomposition method, the Reynolds stress distributions associated with random fluctuation and coherent motion can also be deduced. It is found that both periodic and random Reynolds stresses contribute significantly to the total Reynolds stresses. The peaks of Reynolds stress distributions occur where the centers and saddles are passing.

Key Words: laser doppler velocimeters, phase-averaged technique, co-rotating disks.

I. INTRODUCTION

Hard disk drives are used extensively as data storage devices in computers. A number of technological advances have led to rapid improvements in disk storage characteristics. An increase in rotational speeds of disks and reductions of both track widths and flying height of magnetic head air bearings have enlarged the storage capacity effectively. However, obstacles arise because of the mechanical limitations associated with system reduction and technological advances. Thermal expansion of disks caused by nonuniform temperature distributions can result in exceeding the positioning tolerances of the magnetic heads relatively. Particulates generated by wear can interfere with the flight of recording heads and then cause poor signal-to-noise performance or head collapse. Large-scale fluid structures between disks can also modify the flight of the heads by exciting vibrational modes of the head-suspension-arm or disk flutter. The flow field is a key factor in the

performance of disk drives. In particular, it is necessary to understand the large scale oscillating flow structure induced by the rotation of disks and vortex shedding from the head-suspension-arm, which might cause alignment inaccuracies of the read-write magnetic heads. The flows with and without the arm are of current interest, and the latter isis the topic ofinterest in the present the present study.

The early visualization experiments of Lennemann (1974) and Kaneko *et al.* (1977) provided valuable qualitative insight concerning the influence of configuration geometry on the flow between rotating disks. Using aluminum particles as light scattering agents, Lennmann visualized the motion of water between a pair of centrally clamped co-rotating disks in an axisymmetric enclosure. The experiments revealed the presence of horizontal roll vortices in the form of equiangular spirals embedded in the disk boundary layer. The core of the flow in the space between the disks was indented periodically into the shape of a regular polygon. The rotational speed of the polygon structure was observed to be approximately 80% of the disk rotation speed. Kaneko *et al.* (1977) performed experiments in water and air to visualize the flow between co-rotating disks in a disk pack. At low rotational speeds in water, they observed indentations in the core flow, which

*Corresponding author. (Tel/Fax: 886-2-23634701; Email: ymchen@ccms.ntu.edu.tw)

S. C. Wu is with the Department of General Education, National Defense University, Taoyuan, Taiwan 325, R.O.C.

Y. M. Chen is with the Department of Mechanical Engineering, National Taiwan University, Taipei, Taiwan 106, R.O.C.
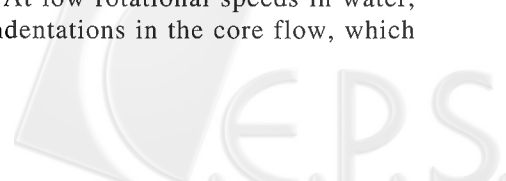
wereis similar to those described previously.

Subsequent flow visualization experiments by Abrahamson *et al.* (1988, 1989) using bromothymol blue indicator in a co-rotating disk water facility clearly showed that the polygon shapes wereare indeed associated with circumferentially periodic and axially aligned vorticity in the flow. This study reported that there existeds a dependence of polygonal shape on the rotating velocity, ..., and the aspect ratio, $S=H/R_2$. The authors found that the number of polygons decreaseds with. and increaseds with S. Under At a low rotational speed of disks,the authors also reported that the vortices made a precession-like motion at a rate of 75% of the disk rotation speed relative to the laboratory. Spectral measurements of the flow field were also made by Abrahamson *et al.* (1988, 1989). Dividing the actual frequencies of the spectra by 0.75ω, the results showed peaks in the energy at integral normalized frequencies for various rotational speeds of disks.

Using the laser-Doppler velocimetry technique in airflow, Schuler *et al.* (1990) and Tzeng and Humphrey (1991) measured the circumferential velocity component in the space between a pair of co-rotating disks in an axisymmetric enclosure. The time sequence of velocity displayed distinct sinusoidal-like oscillations. Schuler *et al.* (1990) also reported that there existed five subregions in the flow field. Tzeng *et al.* (1991) used a high repetition rate copper-vapor laser to illuminate aerosol airflow between co-rotating disks. By means of image processing techniques, Tzeng *et al.* (1991) were able to report on the number of sides of the polygonal interface at high disk speeds, and confirmed the agreement of the inscribing radius of the polygonal structure, evaluated by flow visualization and LDV measurement.

By illuminating the micro-sized mineral oil droplets with a laser sheet, Humphrey and Gor (1993) visualized the cross-stream flow in an experimental apparatus similar to that used by Schuler *et al.* (1990). Experiments showed that the number of vortices decreaseds in a stepwise manner with increasing Reynolds number.

Humphrey *et al.* (1995) numerically investigated the unsteadystreamlined motion of a constant property fluid in the unobstructed space between disks corotating in a fixed cylindrical enclosure using a time-explicit algorithm. The numerical results of Iglesias and Humphrey (1998) confirmed a symmetrical pair of counter-rotating vortices in the cross-stream (r–z) plane. They suggested that the most interesting numerical results correspond to the two- and three-dimensional unsteady case calculated by Humphrey *et al.* (1995) for the experimental conditions investigated by Schuler *et al.* (1990). Their Ccalculations also showed also that the number of vortices
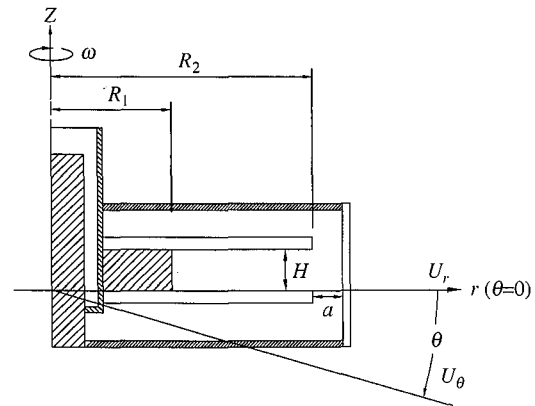

Fig. 1 The test section and coordinate system

decreaseds in a stepwise manner with increasing Reynolds number. Detailed reviews on rotating disk flows with particular emphasis on configurations pertaining to disk storage systems in computer industry have been made by Abrahamson *et al.* (1991) and Humphrey *et al.* (1991).

Although experimental measurements have been made in the above-mentioned studies, the unsteady aspects of the oscillatory flow structure induced by shrouded co-rotating disks are still not well understood. Especially, various quantities caused by oscillatory/turbulent motions of fluid which play the roles of Reynolds stresses in Eqs. (2) - (3) are not well studied yet. In this regard, a measuring technique employing two Laser Doppler Velocimeters (LDV) together with the phase-averaged method were developed to accomplish time-resolved measurements of periodic flow structures induced by shrouded corotating disks in the present study.

II. EXPERIMENTAL PROCEDURES

1. Apparatus and LDV Instrumentation

The experimental model consisted of a motorized test section fixed to an inertial test stand. Its associated coordinates are shown schematically in Fig. 1.

Two rigid disks of outer radius R_2=187.5 mm were concentrically clamped on a hub. The disks were both made of transparent Plexiglas and of thickness b=10 mm. A spacer ring of height H=17.38 mm and radius R_1=59.4 mm was used to separate the disks in the spindle axis direction (z direction). The test section shroud was also made of transparent Plexiglas with an axisymmetric inner wall and radius of R_2+a=189.5 mm. Pure water was used as the working fluid in the experiment. MgO particles with a diameter of about 1.2 μm, were adopted as seeding

material in the LDV measurements.

The principle and practice of laser-Doppler anemometry have been introduced elsewhere, e.g. Durst *et al.* (1981). Only the LDV systems with direct relevance to the present study are introduced here. Two laser velocimeters, an LDV and a Phase Doppler Particle Analyzer (PDPA), were utilized in order to carry out phase-averaged measurements. The schematic of the optical arrangement is shown in Fig. 2. The two-component fiber-optic LDV system worked in a forward scattering mode during the measurements. The optical module consisted of the following components: a TSI Model 9201 Colorburst Multicolor Beam Separator, four Model 9271 couplers, an argon-ion laser (Coherent Innova 90, 2W), a probe with front collimating lens of 350 mm focal length, a single-mode polarization-preserving fiber, a Bragg cell, two pinhole filters and two photomultiplier optics sections. The associated electronics included two photomulipliers, two electronic frequency shifters, three TSI 1990C counter processors, a TSI-MI990 buffer interface.

The PDPA system consisted of five major components: transmitter, receiver, signal processor, motor controller box, and a computer. The Aerometrics model XMT-1100-4S transmitter was used to generate two equal intensity laser beams and to focus them to an intersection point that formed the measurement region. The transmitters contained a Spectra-Physics model SP-106, 10mW, and polarized helium-neon laser. Optical components within the transmitter served to focus, partition, and collimate the laser beam. A beamsplitter with radial diffraction grating helped to produce a frequency shift on measured particle signals. The Aerometrics model MCB-7100-1 motor controller was used to monitor and control the frequency shift. The receiver model RCV-2100 collected the light scattered from seeding particles. The receiver was then connected to the PDP-3100 signal processor with 2 μs resolution to process the Doppler signals. The analog output of the PDP-3100 signal processor was transmitted to the TSI counter processor.

2. Measurement Technique and Data Reduction

The rotation speed of disks was fixed at 133rpm in the present study. By using the radius of the disk as the characteristic length and the disk tip speed as the reference velocity, the Reynolds number was calculated to be 5.25×10^5.

During the measurements, the PDPA probe was fixed at a specific position ($r^* = 0.75$, $Z/H = 0.5$) where the circumferential velocity power spectra had peak values. To investigate the vortical structures, all of the LDV measurements were made in a quarter of the

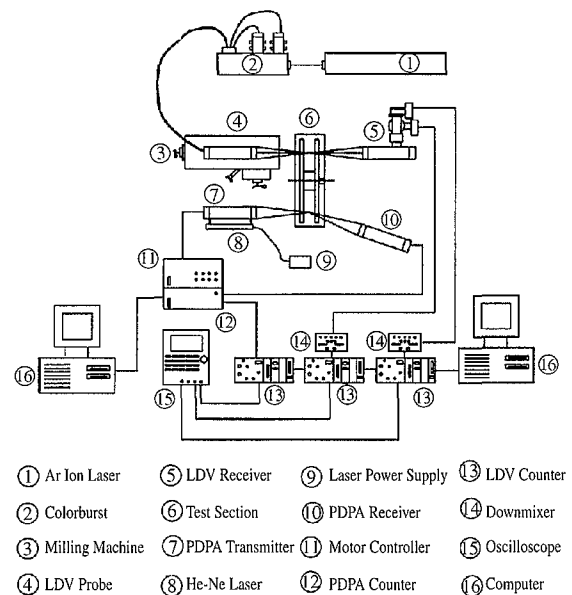| ① Ar Ion Laser | ⑤ LDV Receiver | ⑨ Laser Power Supply | ⑬ LDV Counter |
② Colorburst	⑥ Test Section	⑩ PDPA Receiver	⑭ Downmixer
③ Milling Machine	⑦ PDPA Transmitter	⑪ Motor Controller	⑮ Oscilloscope
④ LDV Probe	⑧ He-Ne Laser	⑫ PDPA Counter	⑯ Computer

Fig. 2 LDV systems

center plane between the two co-rotating disks. In the measurement domain there were totally 4096 points.

The PDPA probe was kept at the specific position as phase reference while the LDV probe was translated in the measurement domain by a three-axis translation stage with an uncertainty of 0.02 mm. Doppler burst signals detected from PDPA and LDV were transferred to the LDV counters, which worked in coincident mode under the control of the TSI MI-990 interface module. A coincident time window length (0.1 ms) was set in the MI-990 interface module to test the synchronization of burst signals detected by PDPA and LDV. The burst signals were processed to compute the Doppler shift frequency, as the time intervals of signals detected by PDPA and LDV were lower than the coincident time window length. Data of Doppler shift frequency was then transferred to a personal computer via a DMA interface card. The velocity values were further calculated and then the time sequence was stored. The coincident data rate was kept at about 2000 Hz as the measurement was made, which was high enough to resolve the periodic motion of vortical structure with 5.08Hz of frequency in the present study. In each measurement, more than 20,000 samples of time sequences of reference point and measuring points were collected, respectively. All of the time histograms of velocity, whether circumferential or radial component, were measured with respect to the same phase reference point. Measurement examples using the phase-averaged method are shown in Fig. 3. A cycle was built between two adjacent crests of time series of U_{ref}, and was then divided into ten phases of equal time interval with phase one and phase ten
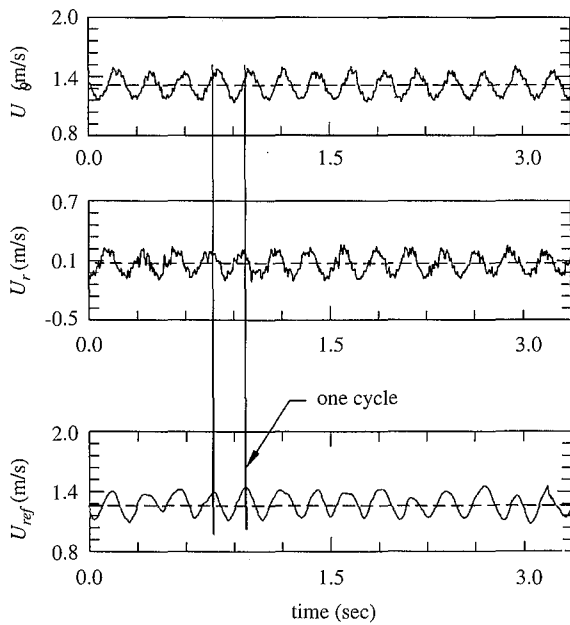
Fig. 3 Typical time records of the circumferential and radial velocity at $r^*=0.40$

Fig. 4 Radial profiles of the power spectra and circumferential mean velocity

corresponding to the crests. Velocity values of U_r and U_θ corresponding to each phase instant defined by U_{ref} were sampled and averaged, respectively. In order to investigate periodic flow fields, a decomposition of velocity proposed by Hussain and Reynolds (1970) was adopted here. The oscillatory flow of co-rotating disks can be taken as a combination of mean components $\overline{u}$, a periodic mean $\tilde{u}$, and a random component u'. By definition, the instantaneous velocity is the sum

$$u = \overline{u} + \tilde{u} + u' \tag{1}$$

According to the analysis by Hussain and Reynolds (1972), the momentum equation taking the average at constant phase has the form,

$$\rho\frac{\partial\langle u_i\rangle}{\partial t} + \rho\langle u_j\rangle\frac{\partial\langle u_i\rangle}{\partial x_j} = -\frac{\partial\langle p\rangle}{\partial x_i} + \mu\frac{\partial^2\langle u_i\rangle}{\partial x_k^2} - \rho\frac{\partial^2[u_i'u_j']}{\partial x_j} \tag{2}$$

The momentum equation for the global mean flow has the form,

$$\rho\overline{u}_j\frac{\partial\overline{u}_i}{\partial x_j} = -\frac{\partial p}{\partial x_i} + \mu\frac{\partial^2\overline{u}_i}{\partial x_k^2} - \rho\frac{\partial\left[\overline{\langle u_i'u_j'\rangle} + \overline{\tilde{u}_i\tilde{u}_j}\right]}{\partial x_j} \tag{3}$$

The bias of calculating global mean velocity was corrected by the method provided by McLaughlin and Tiederman (1973). In situ calibration was carried out with an oscilloscope and the maximum velocity bias
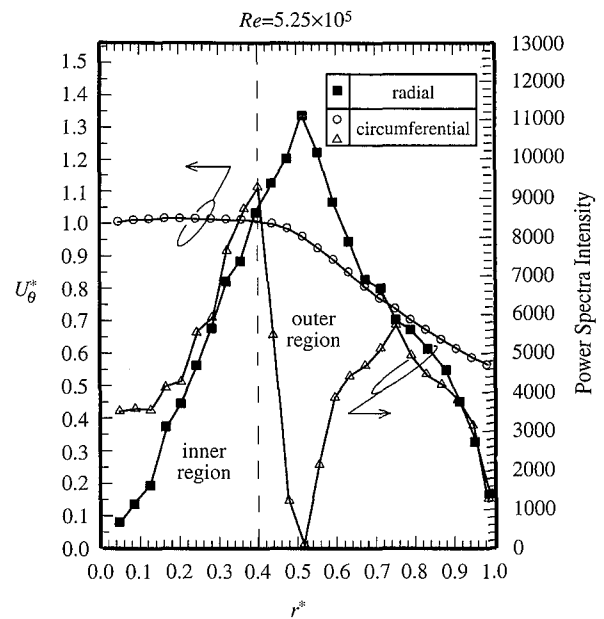
was estimated to be less than 2%. Uncertainties of the phase-averaged velocity and Reynolds stresses were estimated statistically. The maximum uncertainty for phase-averaged velocity was about 4.5% at the 95% probability level. A typical value was about 1.2%. For the six Reynolds stresses, the maximum and typical uncertainties were estimated to be within 5.3% and 3.2%, respectively.

III. RESULTS AND DISCUSSION

1. The Mean Velocity Profile

Figure 4 shows the ensemble-averaged circumferential velocity at the midplane between the disks for $S=0.09$. The values of circumferential velocities were normalized by the local disk speed. A horizontal dashed line was plotted in Fig. 4 to represent the local disk speed ($U_\theta/r\omega$)=1. Two regions can be easily identified from the Fig. 4. In the first region (r^* <0.4), the normalized circumferential velocity U_θ^* approximates to 1. This indicates that the fluid rotates at the same speed as the disks do. This region is the so called solid body rotation region. Similar results were also found by Abrahamson *et al.* (1989) and they called this region the inner region, and the other region the outer region. In the outer region (r^*> 0.4), the normalized circumferential velocity decreases linearly from 1 to 0.57. The interface of the two regions is located at r^*=0.4. As can be seen, good agreement can be found between the present results and Abrahamson *et al.* (1989)
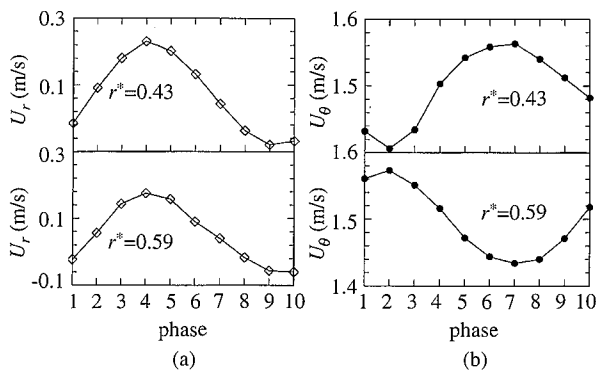
Fig. 5   Phase-averaged of velocities at different phases (a) radial velocity, (b) circumferential velocity

2. Power Spectra Analysis

Figure 4 displays also the radial spectral intensity distributions of the circumferential as well as radial velocity. The spectral intensity of the radial velocity increases with r^* at first, reaches a maximum value at $r^*=0.51$, and then decreases to a weak value at $r^*\approx1$. The radial velocity is most energetic at r*≈ 0.51, and its spectral intensity displays good symmetry to $r^*=0.51$.

On the contrary, spectral intensity distribution of the circumferential velocity is quite different from that of radial velocity. Their two local maxima can be found. The first maximum is located at $r^*=0.4$. This place is also the interface of the inner and outer regions as discussed previously. The second local maximum occurs at $r^*=0.75$, which is also near center of the vortical structures. This will be demonstrated later in this chapter. From the above discussions, it is clear that the circumferential velocity is more energetic at the interface of the inner region and the outer region and also near the center of the vortical structure.

It is interesting to note that the spectral intensity of circumferential velocity is almost zero at $r^*=0.51$. This implies that circumferential velocity does not oscillate there. In Figs. 5(a) and 5(b), curves of velocity that taking phase-averaged velocities at for different ten phases were sketched at the positions $r^*=0.43$ and $r^*=0.59$ as an example. These two points are symmetric to the position $r^*=0.51$. As shown in Fig. 5(a), the radial velocity at these two locations reached crest and base at the same time in a cycle. That is, phase angles of radial velocity are nearly zero between these two points. On the contrary, phase angles of circumferential velocity between these two points are almost 180° at each phase instant as shown in Fig. 5(b). Since the circumferential velocity points symmetric to $r^*=0.51$ are completely out of phase, hence oscillation is eliminated at $r^*=0.51$.

The results of radial and circumferential velocity power spectra show peaks in energy at intergral normalized frequency $f^*=3$ as the actual frequencies of the spectra are normalized by 0.77 times the disk rotational frequency (see Fig. 6). The value of the normalized frequency is the same as the number of vortical structures observed in the reconstructed streamline patterns, as shown in Fig. 8. This indicates that the flow oscillations result from the periodic passage of flow structures.

3. Phase-averaged Results and Sstreamline Patterns

Ten velocity vector fields (each representing 4000 velocity vectors) have been plotted for the case studied here but not all of these will be presented owing to the volume of material involved. Fig. 7 shows the phase-averaged vector fields (Figs. 7(a) and (b)) and the streamline pattern (Fig. 7c) for one of the ten phases. The vector field (Fig. 7b) and streamline pattern (Fig. 7c) are depicted as seen by an observer moving at a reference velocity 0.77ω.

Some other reference velocities were also tested to help identify the streamline pattern. It was found that the vortical structures were not recognized at a higher reference speed. On the contrary, the vortical structure located in the solid-body rotation region at a lower reference speed. It was obviously unreasonable. The appropriate rotational speed was found to be about $(0.77\pm0.04)\omega$. This agrees well with the value of 0.75ω as reported by Abrahamson et al. (1989).

Figures 8(a) to 8(j) represent the streamline patterns at ten phases during the passage of one vortex. Three distinct regions can be identified from the streamline patterns. The solid-body rotation region sustains the dimensionless radial position from $r^*\cong0$ to 0.4, whereas the vortical structure region is from $r^*\cong0.4$ to 0.9, and the shrouded boundary layer region from $r^*=0.9$ to 1. There are totally three vortical structures in the whole flow region.

4. Momentum Transport

In order to quantify the contributions that the flow structures make to the Reynolds stresses, critical points should first be characterized.

When flow patterns are viewed in an appropriate frame of reference, they reveal a number of critical points as shown in Fig. 8. These are points where the velocity components are zero and the streamline slope therefore indeterminate. Identification of critical points is also helpful to discuss the dynamic behavior of vortices. In the present work, the critical points were determined by the method proposed by
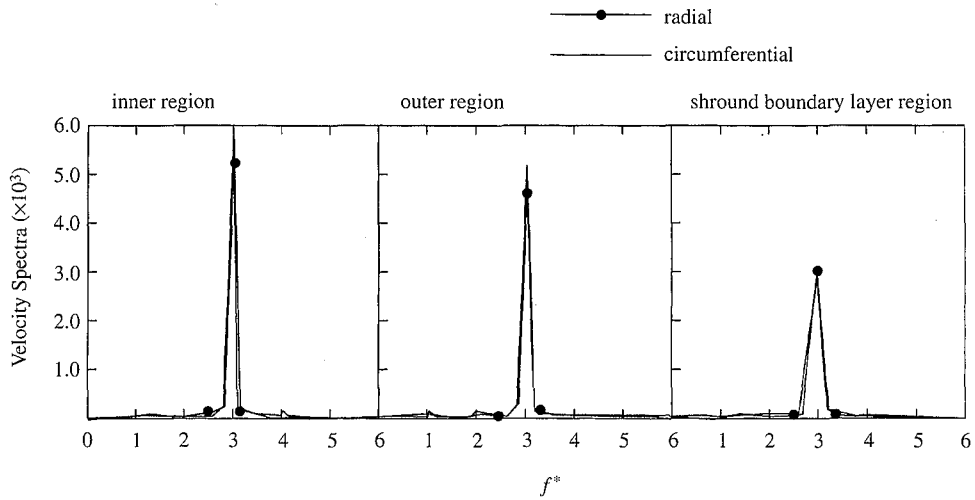
Fig. 6 Normalized spectra of radial/circumferential velocity fluctuation at different radial position
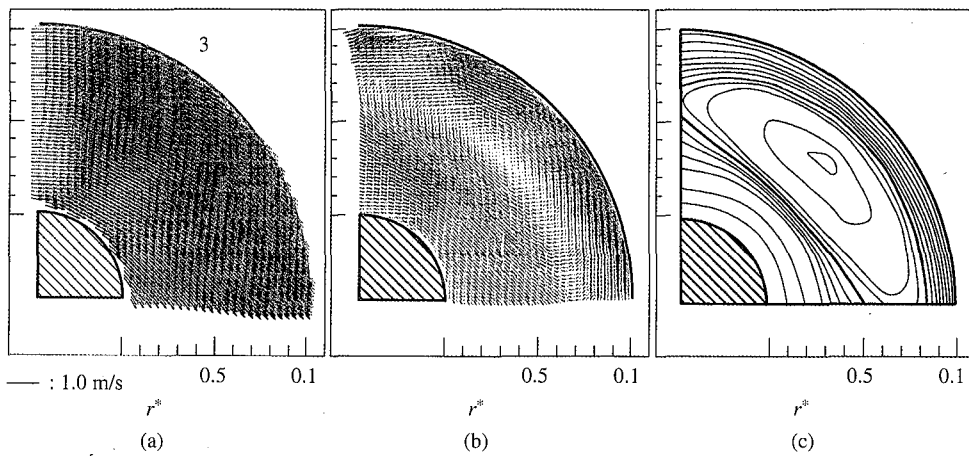
Fig. 7 Velocity vector and streamlines pattern velocity vector (raw data), (b) velocity vector (observed at a reference velocity of 0.77ω), (c) streamlines pattern (observed at a reference velocity of 0.77ω)
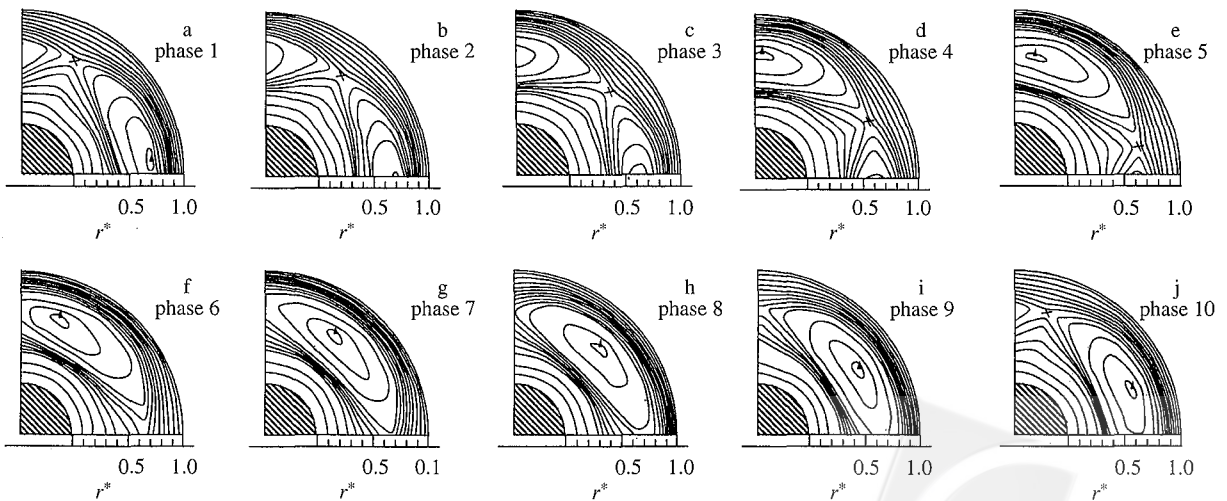
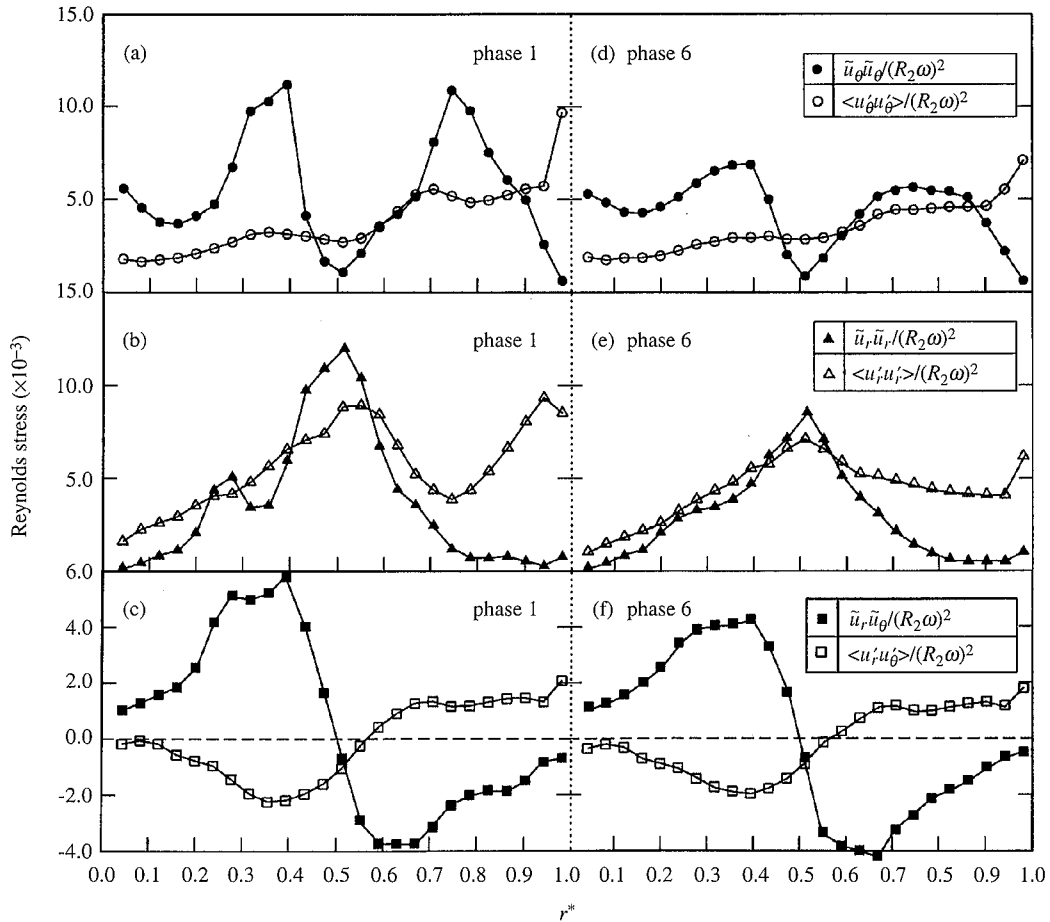Fig. 8 Contour plots of stremlines during passage of one vortex (contour interval 0.15)

Fig. 9 Periodic and random Reynolds stresses distributions at phase 1 and phase 6

Zhou and Antonia (1994). The saddle point (×) and the center point (▲) of the flow are marked in Fig. 8. The saddle and center points of a complete vortex can be observed. As shown in Fig. 7(b), the vortex rotates clockwise.

From the viewpoint of the mean flow as described by Eq. (3), Reynolds stresses are associated with both the periodic and the random motions. These stresses are resolved as functions of radial position and phase from the measurements. In order to discuss the momentum transport, Reynolds stresses distrubutions are shown in Fig. 9. Only the distributions at two phases are depicted here for the sake of brevity. It displays the six Reynolds stresses distributions at phase 1(Fig. 9a. $\tilde{u}_\theta \tilde{u}_\theta$ and $<u'_\theta u'_\theta>$; Fig. 9b $\tilde{u}_r \tilde{u}_r$ and $<u'_r u'_r>$; Fig. 9c, $\tilde{u}_r \tilde{u}_\theta$ and $<u'_r u'_\theta>$) and phase 6 (Fig. 9d. $\tilde{u}_\theta \tilde{u}_\theta$ and $<u'_\theta u'_\theta>$; Fig. 9e $\tilde{u}_r \tilde{u}_r$ and $<u'_r u'_r>$; Fig. 9f, $\tilde{u}_r \tilde{u}_\theta$ and $<u'_r u'_\theta>$). In these figures, the radial distributions at $\theta=0$ are demonstrated.

Figure 9(a) is a plot for $\tilde{u}_\theta \tilde{u}_\theta$ and $<u'_\theta u'_\theta>$. The values of $\tilde{u}_\theta \tilde{u}_\theta$ are double peaked at $r^*=0.4$ and $r^*=0.75$. The first crest is located at $r^*=0.4$, where the

interface of the inner and outer regions is also situated. Analysis of power spectra reveals, also, that U_θ is most energetic at the point $r^*=0.4$. A large amplitude of U_θ causes large $\tilde{u}_\theta$ and contributes more to $\tilde{u}_\theta \tilde{u}_\theta$.

The second peak occurs at $r^*=0.75$. The center point is also observed near $r^*=0.75$ at phase 1 as shown in Fig. 8. That particular point is the vortex center and is also one of the most energetic spots for U_θ velocity. The rotational motion which generates peaks in $\tilde{u}_\theta \tilde{u}_\theta$ at $r^*=0.4$ and $r^*=0.75$, and a positive $\tilde{u}_\theta$ and a negative $\tilde{u}_\theta$ relative to the mean at these locations, is caused by the occurrence of completely out of phase U_θ velocity, as depicted in Fig. 5. At the point $r^*=0.51$, $\tilde{u}_\theta \tilde{u}_\theta$ is nearly zero since U_θ does not oscillate there. The value of $\tilde{u}_\theta$ is nearly zero and makes no contribution to $\tilde{u}_\theta \tilde{u}_\theta$.

Similar distribution for periodic Reynolds stresses was also reported by Cantwell and Coles (1983) and Matsumura and Antonia (1993) in studying near wake flow behind a circular cylinder. In their measurements, the streamwise Reynolds stress $\tilde{u}\tilde{u}$ was nearly zero on the cylinder centerline.

There were also two peaks of streamwise Reynolds stresses generated on either side of the center line of the cylinder, corresponding to negative $\tilde{u}$ and positive $\tilde{u}$, respectively.

Random circumferential fluctuation $<u'_\theta u'_\theta>$ is shown in Fig. 9(a). The quantity $<u'_\theta u'_\theta>$ is small and nearly constant as $r^*<0.6$. It slightly increases from $r^*=0.6$ to $r^*=0.7$, and then remains approximately constant again until $r^*=0.9$. As $r^*>0.9$, $<u'_\theta u'_\theta>$ increases quickly, and then peaks near the shroud.

Fig. 9(b) shows the behavior of $\tilde{u}_r\tilde{u}_r$ and $<u'_r u'_r>$ along the dimensionless radial positions at phase 1. The distributions of $\tilde{u}_r\tilde{u}_r$ and the radial velocity power spectra (see Fig. 4) are quite similar in shapes and peak at the middle point $r^*=0.51$. As r^* increases, the periodicity of the radial velocity fluctuations strengthens till $r^*=0.51$. As $r^*>0.51$ the periodic turbulence level of radial velocity weakens with increasing r^*. Around spindle hub and enclosure shroud, values of $\tilde{u}_r\tilde{u}_r$ are almost zero since solid walls limit periodic fluctuations of radial velocity. Random fluctuation of radial velocity $<u'_r u'_r>$ is exhibited at phase 1 in Fig. 9(b). The turbulent level reinforces as r^* increases from $r^*=0$ to 0.51. The distribution of $<u'_r u'_r>$ double peaks at $r^*=0.51$ and $r^*=0.95$. A local minimum appears at r*=0.75 which is also the region center point. In the region as $r^*<0.75$, the distribution of $<u'_r u'_r>$ is quite similar to that of $\tilde{u}_r\tilde{u}_r$. As $r^*>0.75$, $\tilde{u}_r\tilde{u}_r$ approaches to zero because the periodicity of radial velocity iswas reduced under the shroud restriction. On the contrary, random fluctuation $<u'_r u'_r>$ is enlarged because of the rigid wall effect.

In order to discuss the contributions of the saddle point region to the Reynolds stresses, the case at phase 6 is discussed. Fig. 9(f) shows the two contributions of the Reynolds shear stresses at phase 6. The stresses associated with the periodic motion exhibit consistent asymmetry about the point $r^*=0.51$. The periodic term, $\tilde{u}_r\tilde{u}_\theta$, displays a positive local maximum near $r^*=0.4$ and a negative local minimum at $r^*=0.6$. The positive maximum is located at the interface of the inner and outer regions as discussed before, while the negative minimum exists near the saddle point region as depicted in Fig. 8.

In the vortical region ($0.4<r^*<0.9$), the sign of the shearing stress is such as to produce a rapid flux of circumferential momentum away from the circumferential direction and toward the radial interior of the turbulent region. Reynolds shearing stress $<u'_r u'_\theta>$ caused by random fluctuation is also displayed in Figs. 9(f) and 9(c). The vortical motion yields $<u'_r u'_\theta>$ a sign opposite to that of $\tilde{u}_r\tilde{u}_\theta$. A negative local minimum of $<u'_r u'_\theta>$ occurs at $r^*=0.4$. Then, the value of $<u'_r u'_\theta>$ begins to increase as r^* increases and reaches a local maximum at $r^*=0.65$. Under the influence of
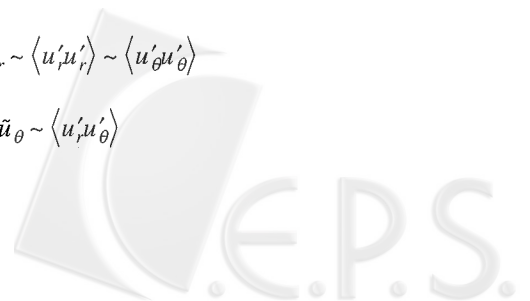
rotational disk tip and the fixed shroud, $<u'_r u'_\theta>$ were amplified and remain nearly a constant value in the region as $r^*>0.65$. The maximum of $<u'_r u'_\theta>$ in absolute value occurs near the shroud ($r^*=1.0$) because of the rigid wall effect.

IV. CONCLUSIONS

The coherent flow structures and their dynamics between a pair of shrouded co-rotating disks are investigated in the present study. Two laser Doppler anemometers together with the phase-averaged method were applied to the flow measurements. In addition to power spectra data, the phase-resolved flow fields as well as the various Reynolds stress distributions are reported in detail. These may provide a basis for numerical verification. Major conclusions are summarized as follows:

(1) Three distinct flow regions can be quantitatively identified from the reconstructed streamline patterns. They include the inner region near the hub, the vortical region (outer region) and the shroud boundary layer region.

(2) The power spectral analysis showed peaks in the energy are at the same integral normalized frequency. The value of the normalized frequency is the same as the number of vortical structures observed in the reconstructed streamline patterns. This indicates that the flow oscillations result from the periodic passage of flow structures.

(3) The center points are associated with the maximums of the periodic Reynolds normal stresses, while the saddle points correspond to extreme of the periodic Reynolds shearing stresses.

(4) Besides the critical points, extremes of the periodic Reynolds stresses exist also at the interface of the inner and outer regions.

(5) The periodic Reynolds normal stresses show symmetry, but, the periodic Reynolds shearring stresses, asymmetry, with respect to the middle point.

(6) The distributions of the periodic Reynolds normal stresses are similar to those of the power spectra intensities of the circumferential/radial velocities. The periodic Reynolds normal stresses seem to play a dominant role in the oscillating flow.

(7) Both the periodic Reynolds stresses and random Reynolds stresses are significant and contribute to the momentum transport in the flow between rotating disks. Their order of magnitude can be stated as follows:

$$\tilde{u}_\theta\tilde{u}_\theta \sim \tilde{u}_r\tilde{u}_r \sim \left<u'_r u'_r\right> \sim \left<u'_\theta u'_\theta\right>$$

$$\gg \tilde{u}_r\tilde{u}_\theta \sim \left<u'_r u'_\theta\right>$$

ACKNOWLEDGEMENTS

NOMENCLATURE

a	distance between disk tip and shroud
b	thickness of disks
f^*	normalized frequency
f_s	dominantdominate frequency of power spectra
H	axial distance between disks
N	numbers of polygonal structures
r	radial coordinates for the system
r^*	dimensionless radial coordinates $=(r-R_1)/(R_2-R_1)$
R_1	radius of hub
R_2	radius of disks
Re	Reynolds number $=(R_2^2\omega)/v$
R_i	radius of inscribing circle of polygon structure
S	dimensionless axial distance of disks $=H/R_2$
U, u	velocity
U_r	radial velocity component
U_{ref}	circumferential velocity of the reference point
$U_{\theta*}$	circumferential velocity component
U_θ	normalized circumferential velocity $=U_\theta/r\omega$
$\overline{u}$	global mean of u, streamwise mean velocity
$\tilde{u}$	periodic fluctuation away from $\overline{u}$, streamwise periodic fluctuation velocity
u'	random fluctuation away from $\tilde{u}$
$\overline{u}_r$	global mean of U_r
$\tilde{u}_r$	periodic fluctuation away from $\overline{u}_r$
u'_r	random fluctuation away from $\tilde{u}_r$
$\overline{u}_\theta$	global mean of U_θ
$\tilde{u}_\theta$	periodic fluctuation away from $\overline{u}_\theta$
u'_θ	random fluctuation away from $\tilde{u}_\theta$
$\tilde{u}\tilde{u}$	streamwise Reynolds stress
$\tilde{u}_r\tilde{u}_r$	radial periodic Reynolds normal stresses
$\tilde{u}_r\tilde{u}_\theta$	periodic Reynolds shearing stresses
$\tilde{u}_\theta\tilde{u}_\theta$	circumferential periodic Reynolds normal stresses
$<u'_r u'_r>$	radial random Reynolds normaling stresses (phase average)
$<u'_r u'_\theta>$	random Reynolds shear stresses (phase average)
$<u'_\theta u'_\theta>$	circumferential random Reynolds normal stresses (phase average)
Z	axial coordinates for the system
θ	circumferential coordinates for the system
v	kinematic viscosity
ω	rotating speed of disks

REFERENCES

Abrahamson, S. D., Koga, D. J., and Eaton, J. K., 1988, "Flow Visualization and Spectral Measurements in a Simulated Rigid Disk Drive," *IEEE Transactions Computational, Hybrids and Manufacturing Technology*, Vol. 11, No. 4, pp. 576-584.

Abrahamson, S. D., Eaton, J. K., and Koga, D. J., 1989, "The Flow between Shrouded Co-rotating Disks," *Physics Fluids A*, Vol.1 , No. 2, pp. 241-251.

Abrahamson, S. D., Eaton., J. K., and Chang, C., 1991, "Flow Structure in Head-Disk Assemblies and Implications for Design," *Advances Information Storage Systems*, Vol. 1, pp. 111-132.

Cantwell, B., and Coles, D., 1983, "An Experimental Study of Entertainment and Transport in the Turbulent Near Wake of a Circular Cylinder," *Journal Fluid Mechanics,* Vol. 136, pp. 321-374.

Durst, F., Melling, A., and Whitelaw, J. H., 1981, *Principles and Practice of Laser-Doppler Anemometry*, Academic, Lodon.

Humphrey, J. A. C., Chang, C. J., Li, H., and Schuler C. A., 1991, "Unobstructed and Obstructed Rotating Disk Flows: A Summary Review Relevant to Information Storage Systems," *Advances Information Storage Systems*, Vol. 1, pp. 79-110.

Humphrey, J. A. C., and Gor, D., 1993, "Experimental Observation of an Unsteady Detached Shear Layer in Enclosed Co-rotating Disk Flow", *Physics Fluids*, Vol. 5, pp. 2438.

Humphrey, J. A. C., Schuler C. A., and Weber, D. R., 1995, "Unsteady Laminar Flow Between a Pair of Disks Co-rotating in a Fixed Cylindrical Enclosure," *Physics Fluids*, Vol. 7, pp. 1225-1240.

Hussain, A. K. M. F., and Reynolds, W. C., 1970, "The Mechanics of an Organized Wave in Turbulent Shear flow," *Journal Fluid Mechanics*. Vol. 41, pp. 241-258.

Iglesias, Immaculada., and Humphrey, Joseph. A. C., 1998, "Two- and Three-Dimension Laminar Flows Between Disks Co-rotating in a Fixed Cylindrical Enclosure," *International Journal for Numerical Methods Fluids*, Vol. 26, pp. 581-603.

Kaneko, R., Oguchi, S., and Hoshiya, K., 1977, "Hydrodynamic Characteristics in Disk Packs for Magnetic Storage," *Reviews Electoral Commerical Laboratory*, Vol.25, No. 11, pp. 1325-1336.

Lennemann, E., 1974, "Aerodynamic Aspects of Disk Files," *IBM Journal Research Development*, Vol. 18, No. 6, pp. 480-488.

MaLaughlin, D. K., and Tiederman, W. G., 1973, "Biasing Correction for Individual Realization of Laser Anemometer Measurements in Turbulent Flows," *Physics Fluids*, Vol. 16, No. 12, pp. 2082-2088.

Matsumura, M., and Antonia, R. A., 1993, "Momentum and Heat Transport in the Turbulent Intermediate Wake of a Circular Cylinder," *Journal Fluid Mechanics*, Vol. 250, pp. 651-668.

Orloff, K. L., and Olson, L. E., 1982, "High-Resolution LDV Measurement of Reynolds Stress in Boundary Layers and Wakes," *Journal American Institute Aeronautics and Astronautics.* Vol. 20, pp. 624-630.

Reynolds, W. C., and Hussain, A. K. M. F., 1972, "The Mechanics of an Organized Wave in Turbulent Shear flow. Part 3. Theoretical Models and Comparisons with Experiments," *Journal Fluid Mechancis*, Vol. 54, pp. 263-288.

Schuler, C. A., Usry, W., Weber, B., Humphrey, J. A. C., and Greif, R., 1990, "On the Flow in the Unobstructed Space between Shrouded Co-rotating Disks," *Physics Fluids A*, Vol. 2, No. 10, pp. 1760-1770.

Tzeng, H. M., Munce, A. C., and Crawforth, L., 199 1, "Quantitative Airflow Visualization between Shrouded Co-rotating Disks," *ASME Experimental Numerical Flow Visualization*, Vol. 128, pp. 141-147.

Tzeng, H. M., and Humphrey, J. A. C., 1991, "Co-rotating Disk Flow in an Axisymmetric Enclosure with and without a Bluff-body," *International Journal of Heat and Fluid Flow*, Vol. 12, No. 3, pp. 194-201.

Usry, W., Schuler, C., Humphrey, J., and Greif, R., 1990, "Unsteady Flow Between Co-rotating Disks in an Enclosure with an Obstruction," *Proceedings of the 5th International Symposium on Application of Laser Techniques to Fluid Mechanics*, Lisbon, Portugal.

Zhou, Y., and Antonia, R. A., 1994, "A Study of Properties near Critical Points in the Near Wake of a Circular Cylinder," *Applied Scientific Research*, Vol. 53, pp. 249-261.